International Journal of Solids and Structures 51 (2014) 808–821

Contents lists available at ScienceDirect

International Journal of Solids and Structures

journal homepage: www.elsevier.com/locate/ijsolstr

A numerical study on the deformation and fracture modes of steel projectiles during Taylor bar impact tests

K.G. Rakvåg [a,*], T. Børvik [a,b], O.S. Hopperstad [a]

[a] Structural Impact Laboratory (SIMLab), Centre for Research-based Innovation (CRI), Department of Structural Engineering, Norwegian University of Science and Technology, NO-7491 Trondheim, Norway
[b] Norwegian Defence Estates Agency, Research & Development Department, NO-0103 Oslo, Norway

ARTICLE INFO

Article history:
Received 5 September 2013
Received in revised form 30 October 2013
Available online 16 November 2013

Keywords:
Fracture
Fragmentation
Stochastic finite element method
Taylor bar impact tests

ABSTRACT

A heterogeneous material model based on macro-mechanical observations is proposed for simulation of fracture in steel projectiles during impact. A previous experimental study on the deformation and fracture of steel projectiles during Taylor bar impact tests resulted in a variety of failure modes. The accompanying material investigation showed that the materials used in the impact tests were heterogeneous on scales ranging from microstructure as investigated with SEM to variation in fracture strains from tensile tests. A normal distribution is employed to achieve a heterogeneous numerical model with respect to the fracture properties. The proposed material model is calibrated based on the tensile tests, and then used to independently simulate the Taylor bar impact tests. A preliminary investigation showed that the simulations are sensitive to assumptions regarding the anvil behaviour and friction properties. A flexible anvil and a yield-limited friction law are shown to be necessary to correctly reproduce the experimental behaviour. The proposed model is then shown to be capable of correctly reproducing all fracture modes but one, and also predict critical impact velocities for projectile fracture with reasonable accuracy. Fragmentation at velocities above the critical velocity is not well reproduced due to excessive element erosion. Measures to make the element erosion process more physical are proposed and discussed with their respective drawbacks. The use of a simple fracture criterion in combination with an element erosion technique accentuates the effect of distributing the fracture parameter.

1. Introduction

The Taylor bar impact test, proposed by Taylor (1948), Whiffin (1948) and Carrington and Gayler (1948) as an experimental method to measure the dynamic yield strength of metallic materials, has been a subject for numerical calculations since the early seventies (Wilkins and Guinan, 1973). This coincides with the evolution of hydrocodes and with the implementation of plasticity in both Eulerian and Lagrangian codes in the years prior to this (Johnson and Anderson, 1987). Lagrangian codes are in general better suited for Taylor bar impact test problems because the history dependent behaviour of a material point in plasticity is tracked exactly (Anderson, 1987), even though the possibly large distortion of the mesh may be detrimental for the critical time-step in the simulations.

Subsequent investigations have shown that the usefulness of the Taylor bar impact test as a material characterisation test is minimal, since Taylor's original analysis is too simplified to accurately describe the dynamic yield stress and the final displacements of the specimen (Johnson, 1972). However, previous investigations on the ballistic perforation resistance of armour plates have shown that the projectile may fracture upon impact (Børvik et al., 2003; Dey et al., 2004, 2007). In that sense, the Taylor bar impact test is ideal for investigating the projectile deformation and fracture modes isolated from the target plate behaviour. It has also been shown that computer-aided designs of protective structures with insufficient fracture criteria for the projectile may cause misleading conclusions (Dey et al., 2011). Based on this, a thorough experimental study of the deformation and fracture modes of steel projectiles at three different hardness values, combined with a material investigation including tensile tests and metallurgical studies, was conducted (Rakvåg et al., 2013). The final goal of the present work is to use this new knowledge to predict the critical velocity for projectile failure and the associated loss of penetrating capability, and thus to increase the reliability of computer-aided design of protective structures.

Failure modelling in numerical simulations of ballistic impact problems has been investigated for a long time (Berthoff et al., 1975), but this work has mainly concentrated on fracture in the target. The earliest efforts limited itself to a measured value of a critical stress or strain, whereas contemporary methods often

* Corresponding author. Tel.: +47 95 75 58 35.
E-mail address: knut.gaarder.rakvag@ntnu.no (K.G. Rakvåg).

0020-7683/$ - see front matter © 2013 Elsevier Ltd. All rights reserved.
http://dx.doi.org/10.1016/j.ijsolstr.2013.11.008

employ a cumulative damage function, based on macro-mechanical tests (Johnson and Cook, 1985) or micromechanical analysis (Gurson, 1975). In consideration of dynamic fracture, time dependence is observed (Tuler and Butcher, 1968), which should be accounted for. The time dependence is due to inertia effects on void growth, favouring void nucleation (Antoun et al., 2003).

In the Taylor bar impact test, large strains combined with high strain rates result in adiabatic heating of the material (Johnson et al., 2006). Thus, it is often used as validation of thermoviscoplastic constitutive models such as the Johnson–Cook (1983) and the Zerilli–Armstrong (1987) models. An interesting observation is that Johnson and Cook (1983, 1985) found discrepancies both for the final shape and the damage evolution between their numerical results and experiments. We will show that these discrepancies may be attributed to the stiffness of the anvil and frictional effects which are two simplifications from Taylor's original analysis that are not justified in all cases.

Regarding simulation of fracture in the Taylor bar impact tests, the work of Johnson and Cook (1985) is already mentioned. They did not simulate crack propagation explicitly with element erosion, but observed that their damage model did not predict fracture at the critical impact velocity from experiments. Anderson et al. (2006) obtained the opposite result using a simplified version of the Johnson–Cook damage model. Their numerical simulations predicted failure at lower impact velocities than the experiments. These results highlight some of the difficulties in predicting failure in the projectile in numerical simulations of the Taylor bar impact test.

In Fig. 1 five distinct failure and fragmentation modes in the projectile during the Taylor bar impact test are shown. These are in order of increasing severity: (a) plastic mushrooming without any visible cracking, even though extensive void growth just behind the centre of impact due to hydrostatic tension in the projectile may still occur; (b) tensile splitting on the edge of the mushroomed end due to tensile hoop strains exceeding the material ductility; (c) adiabatic shear cracking either by (1) principal shear fracture where a circular wedge separates or (2) combined spiral shear fracture and tensile splitting where the mushroomed material separates from the impact end of the projectile; (d) petalling initiated by tensile splitting that may cause fragmentation of the petals at the highest impact velocities and (e) full fragmentation initiated by crack growth from one or several shear cracks. Note also that combinations of two or more of these generic modes are likely in real situations.

Teng et al. (2005) recreated numerically three of these fracture modes, namely interior void growth, spiral shear fracture and petalling. They also compared results obtained with the Johnson–Cook fracture criterion with a fracture locus proposed by Bao and Wierzbicki (2004). Based on this they proposed a modification of the Johnson–Cook fracture model in which the fracture strain approaches infinity when the stress triaxiality goes to $-1/3$. They further showed that this modification of the Johnson–Cook fracture model gives fewer eroded elements for simulations of ductile steel projectiles. The latter result was also shown by Xiao et al. (2011) for simulations of a high strength aluminium alloy. In addition, they performed experiments and showed that simulations with a cut-off on the failure strain in the Johnson–Cook model predicted more realistic critical velocities for the various fracture modes. It was also shown that fewer eroded elements gave a better representation of the physical damage modes. In an evaluation of several fracture models for Taylor bar impact tests, Zhang et al. (2011) concluded that a modified Johnson–Cook model with a cut-off criterion or the Cockcroft–Latham (1968) fracture criterion are the best options.

Although it is common to use homogeneous fracture properties in numerical simulations, the stochastic nature of fracture can be deduced already from Leonardo Da Vinci's tensile tests of wire (Lund and Byrne, 2001). This is the earliest scientific material investigation recorded (Timoshenko, 1953), and it has been used in analysis of fracture and fragmentation since around WWII (Mott, 1947). In numerical simulations of fracture, a Weibull distribution, as in the Beremin model (1983), is often used. In the Beremin model, the Weibull distribution of the fracture parameter is coupled with a term V/V_0, where V is the volume represented by the integration point and V_0 is a reference volume. The result of this is that with mesh refinement, the average integration point becomes stronger, but since there are more elements in the refined mesh the probability of failure initiation is the same in the domain regardless of mesh size. With this approach the size effect on failure will be reproduced automatically, since a larger domain increases the possibility for the onset of failure.

The method described above assumes that when the first point in the domain reach failure, it immediately follows that the rest of the structure fails catastrophically (Meyer and Brannon, 2012).

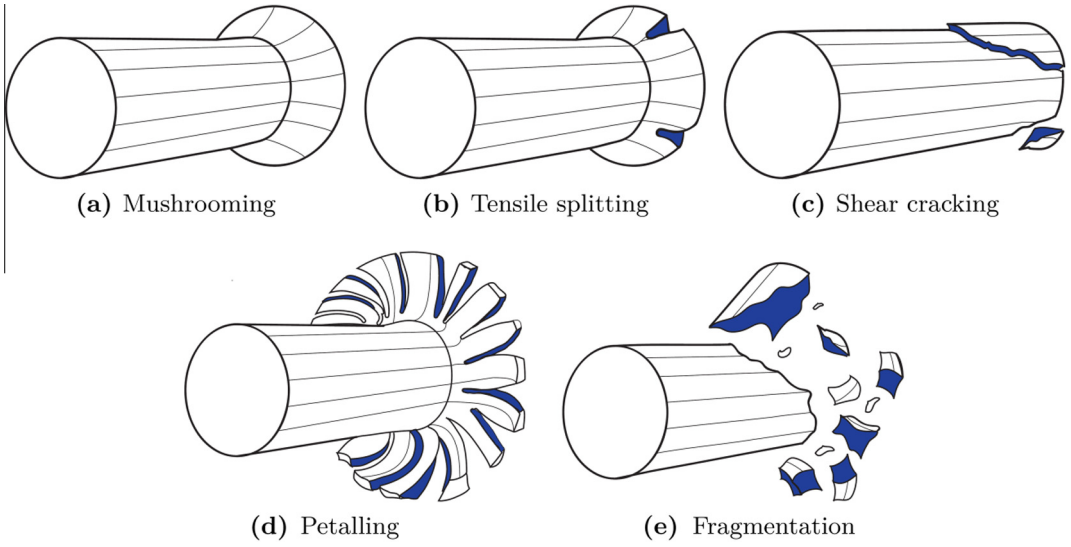

Fig. 1. Deformation and fracture modes in the Taylor bar impact test (Rakvåg et al., 2013).

They further showed both theoretically and through simulations that even for realistic mesh refinements, the term V/V_0 gives a non-physical material representation with an unrealistically strong base material and too few weak spots. Based on this, it seems that a relatively small variation of the fracture parameter, without a volume term, is more appropriate in simulations where the goal is to predict various fracture modes and not only the initiation of fracture. It follows from this approach that failure at a material point does not necessarily result in immediate catastrophic failure, but just a local softening of the material. In this paper, we will thus apply a thermoelastic–thermoviscoplastic constitutive relation where the fracture parameter is a random variable defined by a normal distribution. The normal distribution is chosen here for its simplicity. The aim will then be to investigate if the heterogeneous model gives a better description of the failure process in the Taylor bar impact test.

The paper is organised as follows. A brief summary of the experimental results presented by Rakvåg et al. (2013) is given in Section 2. The constitutive relation will be presented in Section 3 and calibrated in Section 4. In Section 5 the results of the numerical simulations of the Taylor bar impact tests are presented and compared with the results from Section 2. Section 6 presents a discussion on shortcomings of the modelling approach and possible remedies as well as the conclusions of the study.

2. Summary of experimental work

The experimental work used in this paper was presented in detail by Rakvåg et al. (2013), but a short summary of the findings relevant to this paper is provided in the following. All projectiles are made from Arne tool steel (Uddeholm, 2012), but with three different hardness values, i.e. unhardened (UH), hardened to HRC 40 and hardened to HRC 52. All projectiles have a nominal length of 80 mm and a nominal diameter of 20 mm, giving a nominal mass of 197 g. A compressed gas gun was used to accelerate the projectiles into an impact chamber at velocities up to 350 m/s. In the impact chamber the projectile velocity was measured by a laser-based velocity measurement station, which also triggered the high-speed video camera, before the projectile impacted an anvil made of steel hardened to HRC 60. The anvil had a diameter of 100 mm and a length of 50 mm, and was supported by thick high-strength steel plates with no visible deflection in the high speed video recordings.

2.1. Results from Taylor bar impact tests

In Table 1 the experimental results are presented for different combinations of hardness and impact velocity. For the projectiles that did not fracture, deformed diameter and deformed length are presented. For the projectiles that fractured, the fracture mode according to Fig. 1 is presented in the following, while details on the fragment-size distribution are reported in Rakvåg et al. (2013).

For the unhardened projectiles only the projectile with impact velocity of 341.4 m/s fractured, and the highest impact velocity without fracture was 297.2 m/s. Thus, the critical impact velocity for projectile fracture is within this range. The HRC 40 projectiles are found to have a critical velocity in the range between 246.5 and 269.9 m/s, where tensile splitting was observed in the deformed projectile. For impact velocities higher than 269.6 m/s, spiral shear was the dominant fracture mode. All but one of the HRC 52 projectiles fractured upon impact. The projectile with an impact velocity of 124.4 m/s did not fracture. The HRC 52 projectiles with an impact velocity of 153.7 m/s and above fragmented excessively.

In Fig. 2 typical fracture behaviours for the three different hardness values are shown, all at nominal impact velocity of 300 m/s. As seen, the unhardened projectile at 297.2 m/s experiences excessive mushrooming without fracture, while the HRC 40 projectile at 297.7 m/s shows spiral shear fracture with a few fragments. The HRC 52 projectile fragments completely at an impact velocity equal to 296.3 m/s.

2.2. Results from material investigation

Series of quasi-static tensile tests were carried out for all the three materials. Typical true stress vs. true strain curves for the three different materials are shown in Fig. 3. A distinct variation in properties between the three materials is seen, while the fracture strain is found to vary considerably for each material. Dynamic tensile tests performed in a Split-Hopkinson Tension Bar (SHTB) was also performed to investigate the strain rate sensitivity of the unhardened material, and the dynamic flow stress is found to have a log-linear dependence of the strain rate as shown in Fig. 4.

A metallurgical investigation using Scanning Electron Microscope (SEM) on the fracture surfaces from some of the fractured projectiles has also been carried out. In the unhardened projectile all examined surfaces were dimpled, while in the HRC 40 projectile both dimpled and smooth fracture surfaces were found. Dimples in the fracture surfaces are evidence of void nucleation and growth, indicating a ductile fracture process, while a smooth fracture surface is evidence of a brittle fracture process (Dieter, 1988). In the HRC 52 projectiles several different fracture surfaces were found. Fracture surfaces from the front of the projectile were smooth and without any dimples, providing evidence of brittle fracture. Away from the impacting end, the fracture surfaces were dimpled and showed cleavage-like patterns, indicating a quasi-cleavage form of fracture.

3. Constitutive relation

3.1. Scope and limitations

The material is assumed to be isotropic and follow the von Mises yield criterion with non-linear isotropic hardening based on a modified version of the Johnson–Cook constitutive equation which includes thermoelasticity and thermoviscoplasticity (Børvik et al., 2001). Due to the large strains and strain rates expected in the Taylor bar impact tests, the heating caused by plastic work is treated as fully adiabatic. The damage evolution is modelled by the Cockcroft–Latham (1968) fracture criterion, and includes a statistical distribution of the fracture parameter.

3.2. Thermoelastic–thermoviscoplastic constitutive model

Since the material is assumed to be isotropic, the thermoelastic behaviour is defined by Young's modulus E, Poisson's ratio ν and the thermal expansion coefficient α. The thermoelastic coefficients are assumed to be constant, and nominal values for steel at room temperature are adopted in the simulations, cf. Table 2.

In the plastic domain, the von Mises equivalent stress σ_{eq} is given as a function of the equivalent plastic strain ε_{eq}, the equivalent plastic strain rate $\dot{\varepsilon}_{eq}$ and the temperature T as

$$\sigma_{eq} = (\sigma_Y + R(\varepsilon_{eq}))\left(1 + \frac{\dot{\varepsilon}_{eq}}{\dot{\varepsilon}_0}\right)^C \left(1 - \left(\frac{T - T_r}{T_m - T_r}\right)^m\right) \tag{1}$$

where σ_Y is the initial yield stress, R is the isotropic hardening variable, $\dot{\varepsilon}_0$ is a reference strain rate, T_r is the initial temperature and T_m is the melting temperature of the material. The variables C

Table 1
Some experimental results.

Hardness (HRC)	Impact velocity (m/s)	Deformed diameter (mm)	Deformed length (mm)	Fracture mode
UH	126.7	22.5	76.0	Mushrooming
	155.5	23.8	74.0	Mushrooming
	185.5	25.6	71.8	Mushrooming
	196.7	26.6	71.1	Mushrooming
	250.0	30.5	67.0	Mushrooming
	297.2	35.1	62.2	Mushrooming
	341.4	–	–	Spiral shear
HRC 40	132.5	22.1	77.5	Mushrooming
	137.1	22.2	77.4	Mushrooming
	182.8	24.6	75.3	Mushrooming
	201.2	25.9	74.4	Mushrooming
	246.5	28.8	72.2	Mushrooming
	269.6	30.5	70.9	Tensile splitting
	297.7	–	–	Spiral shear
	325.6	–	–	Spiral shear
	356.5	–	–	Spiral shear
HRC 52	124.4	22.5	78.8	Mushrooming
	132.9	–	–	Principal shear
	134.7	–	–	Principal shear
	153.7	–	–	Fragmentation
	201.8	–	–	Fragmentation
	250.5	–	–	Fragmentation
	296.3	–	–	Fragmentation

Fig. 2. High-speed video images from Taylor bar impact tests with nominal impact velocities of 300 m/s. The images show typical impact behaviour for the different hardness values: (a) unhardened projectile with mushroom deformation, (b) HRC 40 projectile with spiral shear and a few fragments, and (c) HRC 52 projectile showing complete fragmentation.

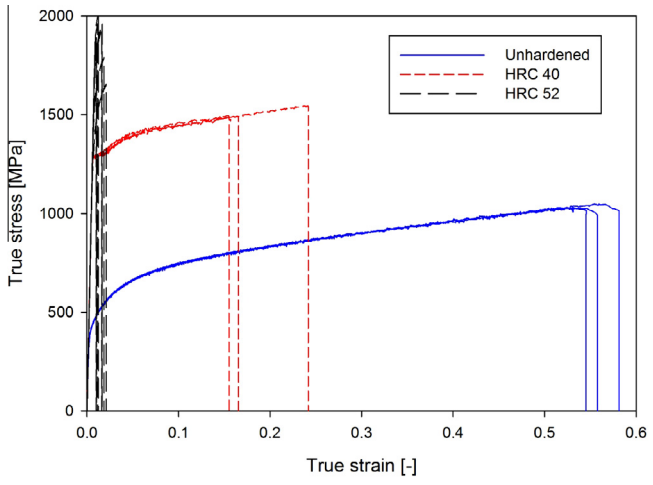

Fig. 3. True stress vs. true strain curves from quasi-static tensile tests on the three different materials used: unhardened, HRC 40 and HRC 52.

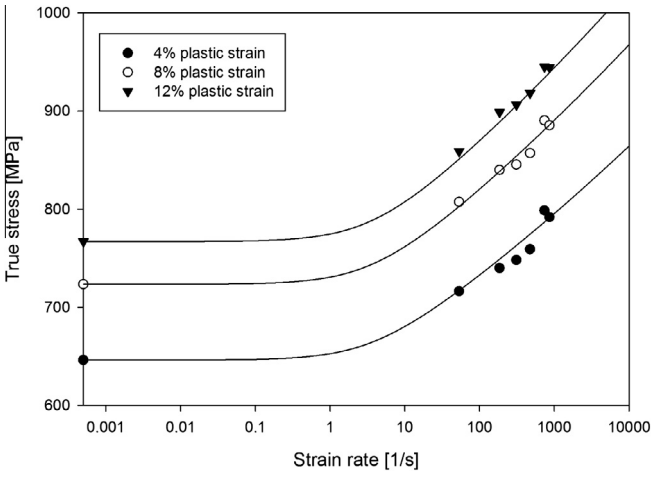

Fig. 4. Dynamic flow stress according to the modified Johnson–Cook relation vs. strain rate on logarithmic scale. Experimental results are plotted with markers for 4%, 8%, and 12% plastic strain.

Table 2
Physical constants for steel.

Thermoelastic constants			Density	Constants related to adiabatic heating			
E [MPa]	ν	α	ρ [kg/m^3]	T_r [K]	T_m [K]	C_p [J/kg/K]	β
210,000	0.3	1.2×10^{-5}	7850	293	1800	452	0.9

and m govern the rate and temperature sensitivity of the hardening, respectively. The isotropic hardening variable R is defined as the sum of two contributions R_1 and R_2 representing different stages in the hardening of the material, viz.

$$R = \sum_{i=1}^{2} R_i(\varepsilon_{eq}) = \sum_{i=1}^{2} Q_i \left(1 - \exp\left(-\frac{\theta_i}{Q_i}\varepsilon_{eq}\right)\right) \tag{2}$$

where Q_i and θ_i are the saturation value and the initial rate of change of R_i, respectively. The temperature increment $\mathrm{d}T$ due to adiabatic heating is obtained in the form

$$\mathrm{d}T = \beta \frac{\sigma_{eq}}{\rho C_p} \mathrm{d}\varepsilon_{eq} \tag{3}$$

where β is the Taylor–Quinney coefficient that represents the proportion of plastic work converted into heat, ρ is the material density and C_p is the specific heat.

3.3. Damage model

Damage is modelled as proposed by Cockcroft and Latham (1968). The damage is accumulated as

$$\mathrm{d}D = \frac{\langle \sigma_1 \rangle}{W_c} \mathrm{d}\varepsilon_{eq} \tag{4}$$

where σ_1 is the major principal stress, $\langle \sigma_1 \rangle = \max(\sigma_1, 0)$ and W_c is the fracture parameter. Fracture is assumed to occur when D equals unity. The fracture parameter W_c is the only random variable in this study, and it is assumed to follow a normal distribution, viz.

$$f(W_c) = \frac{1}{s_{W_c}\sqrt{2\pi}} \exp\left(-\frac{1}{2}\left(\frac{W_c - \bar{W}_c}{s_{W_c}}\right)^2\right) \tag{5}$$

where $\bar{W}_c$ is the mean value and s_{W_c} is the standard deviation. The normal distribution was adopted mainly for its simplicity and lack of data, since the number of tensile tests for each material is not sufficient to determine the appropriate statistical distribution (see also the discussions in Rakvåg et al. (2013)). The Cockcroft–Latham fracture criterion is also chosen for its simplicity, having only one parameter, while still capturing the important feature of increasing fracture strain with decreasing stress triaxiality. Details of the fracture locus of the Cockcroft–Latham criterion as a function of stress triaxiality and Lode parameter can be found in Kane et al. (2011) or Gruben et al. (2012).

4. Calibration of the material model

The constitutive relation and fracture criterion for the three different materials used in this study are calibrated based on the material investigations presented by Rakvåg et al. (2013). The quasi-static tensile tests on smooth axisymmetric specimens were conducted using an in-house measuring devise with two perpendicular lasers that accurately measured the specimen diameter in two directions (denoted d_1 and d_2 in this study) instead of using a traditional extensometer. This ensures that valid stress–strain information is obtained also after possible necking of the specimen, by measuring the minimum cross-section continuously all the way to fracture. The rig is mounted on a mobile frame to always measure the area $A = \pi d_1 d_2/4$ at the minimum cross-section, in addition to the force F measured by the load-cell of the tensile machine. The Cauchy (true) stress is then given directly as

$$\sigma = \frac{F}{A} \tag{6}$$

Note that after necking this represents an average measure of the stress over the minimum cross-section.

The elastic strain can in general not be neglected in the calculation of the logarithmic (true) plastic strain, and especially not in this case since rather brittle materials are included in the study. Thus, assuming plastic incompressibility and a Poisson's ratio ν, the elastic and plastic parts of the radial strain ε_r are related to the longitudinal strain ε_l as

$$\varepsilon_r = \varepsilon_r^e + \varepsilon_r^p = -\nu\varepsilon_l^e - \frac{1}{2}\varepsilon_l^p = -\nu\varepsilon_l^e - \frac{1}{2}(\varepsilon_l - \varepsilon_l^e) \tag{7}$$

Solving this equation for the longitudinal strain gives

$$\varepsilon_l = -2\varepsilon_r + (1 - 2\nu)\varepsilon_l^e \tag{8}$$

Using

$$\varepsilon_r = \ln\frac{d}{d_0} = -\ln\frac{d_0}{d} = -\frac{1}{2}\ln\frac{A_0}{A} \tag{9}$$

and Hooke's law for the elastic strain give the following expression for the longitudinal strain as a function of the measured minimum cross-section area and force

$$\varepsilon_l = \ln\frac{A_0}{A} + (1 - 2\nu)\frac{F}{AE} \tag{10}$$

where E is the elastic modulus of the material.

In addition to the yield stress, the hardening description, the strain rate sensitivity and the damage parameters which were identified for each material, the thermoelastic constants, the density and the constants related to adiabatic heating are required. Nominal values for these parameters are summarized in Table 2.

4.1. Yield stress and work hardening

Based on the tensile tests, parameters for the yield stress and the work hardening were fitted such that the results from numerical simulations of the tensile tests were equal to the curves generated with Eqs. (6) and (10). The true stress–strain curves from the tensile tests are shown in Fig. 3. It is important to note that for the specimens that necked (i.e. the unhardened and HRC 40 specimens), the stress calculated from Eq. (6) is no longer the equivalent stress due to the three-dimensional stress state in the neck. Bridgman's well known solution to the problem is dependent on measurements of the neck radius at the root, which is hard to measure exactly. Both an approximation to the neck radius proposed by Le Roy et al. (1981) and an empirical solution to the entire problem by Mirone (2004) were applied without satisfactorily results.

Instead inverse modelling was adopted to determine the yield and hardening parameters, using the experimentally obtained force vs. diameter reduction curves as targets. For the inverse modelling of the hardening parameters, the optimization tool LS-OPT that interfaces with LS-DYNA (2006) was used to run hundreds of successive simulations of an axisymmetric finite element model

Table 3
Yield stress and hardening parameters for the three different steel qualities used.

	σ_0 [MPa]	Q_1 [MPa]	θ_1 [MPa]	Q_2 [MPa]	θ_2 [MPa]
Unhardened	395	372	1370	240	10776
HRC40	1203	1026	268	201	10225
HRC52	1660	1195	24856	1230	564690

of the tensile tests. A hybrid optimization algorithm was used to successively optimise the hardening parameters based on the mean square error until the numerical stress–strain curves obtained in the form of Eqs. (6) and (10) were converged with the experimental curves. The material parameters from the optimization are summarized in Table 3.

4.2. Damage and fracture criterion

Both the tensile tests and the metallurgical investigations presented by Rakvåg et al. (2013) of the three different materials indicate heterogeneous fracture properties. To include this heterogeneity in the simulation models, the fracture parameter W_c of the Cockcroft–Latham fracture criterion was defined as a random variable with a normal distribution in the subsequent simulations. The fracture parameter was determined through trial and error inverse modelling of the quasi-static tensile tests. All simulations were performed with the IMPETUS Afea Solver (2013). Solid selective-reduced elements, Green–Naghdi stress rate and double-precision are used in the calculations. A mesh size of 0.5 mm × 0.5 mm × 0.5 mm was adopted and no symmetry conditions were utilised. To model fracture, elements were deleted when the first out of the eight integration points reached the critical value of damage.

Ideally, the tensile tests should be repeated until the number is sufficient to determine a proper distribution of the fracture strain. In the preceding experimental work (Rakvåg et al., 2013), a test programme was carried out to determine this distribution for the two hardened materials. The initial test specimens were cut from projectiles after hardening, while the test series to determine the distribution were cut from the unhardened material and then hardened. This was done to avoid micro-cracks due to the spark-eroding process used for the cutting of the hardened materials. However, the difference in size when hardened, giving different cooling times, resulted in different material behaviour for the test series supposed to determine the distribution. Then a new test series with specimens cut from the hardened material was carried out, where the gauge area was polished in an attempt to minimize the influence of the spark-eroding process on the material behaviour. This approach gave somewhat lower fracture strain than the original test series, leaving the true fracture strain unresolved. It was based on this decided to use the deviation of the hardened and then cut test series as an upper bound of the acceptable deviation in fracture strain due to the detrimental effect of the cutting process on the material behaviour. A set of fracture parameters was thus accepted if the mean fracture strain produced was equal to the mean from the experiments, and the deviation of the fracture strain was less than the deviation of the experimental fracture strains. The fracture parameters found by this approach are given in Table 4. It is important to note that the parameter $\bar{W}_c$ is not equal to the parameter W_c in a homogeneous model, due to the statistical variation. Even though the weakest element will not lead immediately to catastrophic failure when it is deleted, the load-carrying area will be reduced and the damage evolution in the vicinity of the deleted element will be amplified.

Table 4
Fracture parameters for the Cockcroft–Latham fracture criterion for the three different materials.

	$\bar{W}_c$ [MPa]	s_{W_c} [MPa]	W_c [MPa]
Unhardened	650	65	535
HRC40	500	80	322.5
HRC52	30	6	22.5

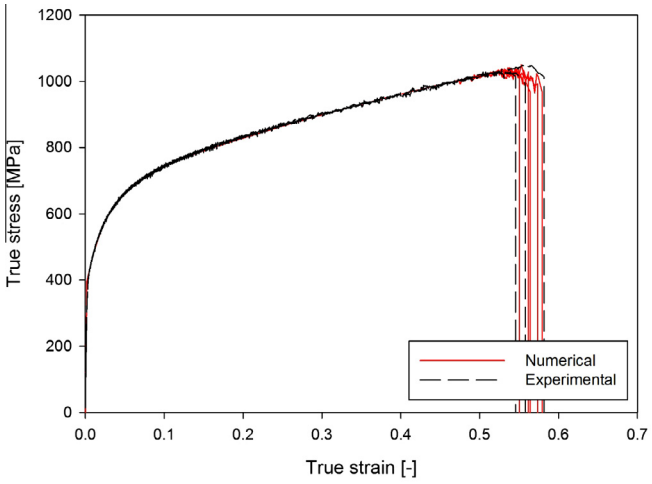

Fig. 5. Comparison of experimental and numerical tensile test results for the unhardened material. The work hardening is well reproduced and the fracture strains from the numerical simulations are bounded by the experimental curves.

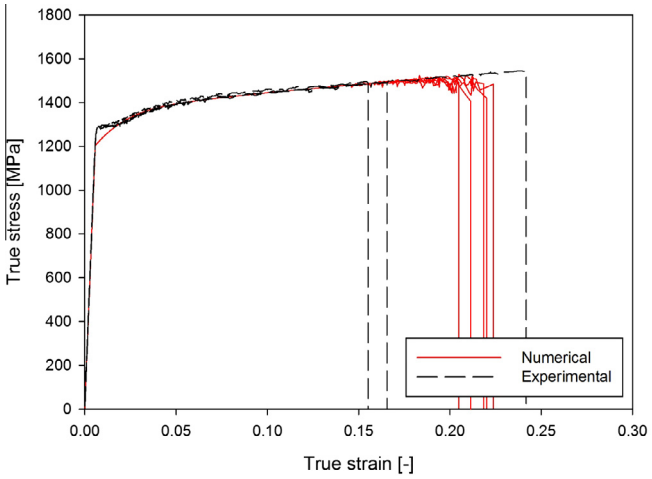

Fig. 6. Comparison of experimental and numerical tensile test results for the HRC 40 material. The work hardening is well reproduced except for the yield plateau, while the fracture strains from the numerical simulations are bounded by the experimental curves.

Five realisations of the tensile test for each material are shown together with the experimental results in Figs. 5–7, where is it seen that the agreement between the experimentally obtained and 3D numerically simulated stress–strain curves validates the hardening parameters obtained through inverse-modelling in Section 4.1. In Fig. 5, the experimental true stress–strain curves for the unhardened material are shown together with the corresponding numerical curves computed in the same way from the nodal displacements at the neck and the boundary forces in the model. The work hardening is reproduced exactly, and the fracture strains are within the bounds of the three experiments. The true stress–strain curves for the HRC 40 material are plotted in Fig. 6. Apart from the initial yield plateau which is not accounted for in this study, the elastic–plastic behaviour is reproduced with sufficient

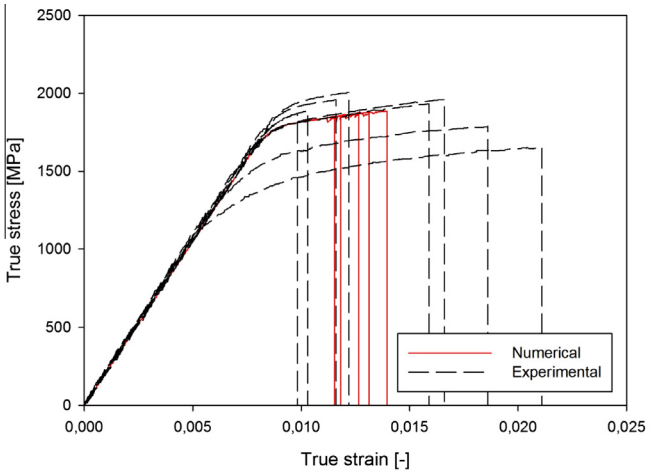

Fig. 7. Comparison of experimental and numerical tensile test results for the HRC 52 material. The numerical model gives results that are well within the material behaviour observed experimentally.

Table 5
Strain rate sensitivity parameters used in the numerical study.

	C [−]	$\dot{\varepsilon}_0$ [1/s]
Unhardened	0.036	3.155
HRC40	0.018	3.155
HRC52	0.00018	3.155

precision, and the numerical fracture strains are well within the obtained results from the experimental tests. Finally, Fig. 7 shows the results from the numerical simulations of the tension test for the HRC 52 material compared with some of the experimental results. Note that the yield stress is assumed to be homogeneous in the simulations even though the yield stress varies in the experiments. It is seen that the chosen yield stress and hardening reproduce the median yield stress and that the numerical fracture strains are bounded by the experimental fracture strains.

4.3. Strain rate sensitivity

In addition to the quasi-static tensile tests for all three materials, dynamic tensile tests were performed for the unhardened material in a Split-Hopkinson Tension Bar (SHTB). As shown by Rakvåg et al. (2013), the ratio between the dynamic flow stress σ_d and the quasi-static flow stress σ_s converges for plastic strains above 4% and up to necking which occurred at about 12% plastic strain. Based on this, the ratio between the dynamic flow stress and the quasi-static flow stress in the Modified Johnson–Cook constitutive relation, i.e.

$$\frac{\sigma_d}{\sigma_s} = \left(1 + \frac{\dot{\varepsilon}_{eq}}{\dot{\varepsilon}_0}\right)^C \tag{11}$$

was fitted to the experimental values between 4% and 12% plastic strain using the method of least squares. The dynamic flow stress according to Eq. (11) is plotted in Fig. 4 for 4%, 8%, and 12% plastic strain. It is seen that the accordance between Eq. (11) and the experimental results are good. The strain rate sensitivity of the HRC 40 and HRC 52 materials was not determined experimentally, but based on previous experience the strain rate sensitivity declines with increasing hardness of the material (Børvik et al., 2009). It was therefore assumed that the strain rate sensitivity parameter C for the HRC 40 material is half of the unhardened material, and that the HRC 52 material only has a minor positive strain rate sensitivity for numerical stability. The parameters used for each material are summarized in Table 5. Since the material behaviour at elevated temperatures was not investigated in this study, the material parameter m governing temperature sensitivity is set to unity, which gives a linear decrease of the flow stress with increasing temperature. Although the strength of steel often shows a non-linear dependence on temperature (see e.g. Børvik et al. (2005)), a linear decrease is a much used assumption that was adopted here (see e.g. Johnson and Cook (1983)).

5. Simulation of Taylor bar impact tests

All numerical simulations of the Taylor bar impact tests were analysed with the IMPETUS Afea Solver (2013), an explicit finite element code for non-linear mechanics. To ensure that the parameters obtained in Section 4 are compatible with the subsequent numerical analyses, the Taylor bar impact tests were modelled exactly as the tensile tests in Section 4. Thus, the mesh is uniform throughout the projectile with a nominal element size of $0.5 \times 0.5 \times 0.5$ mm. The projectiles, which are 80 mm long and 20 mm in diameter, are meshed with 240,000 eight-node linear solid elements. The anvil is meshed with 30,000 eight-node linear solid elements with a nominal size of $2.5 \times 2.5 \times 2.5$ mm. The finite element mesh of the projectile and anvil is shown in Fig. 8. In the simulations with a distributed fracture criterion, a random value of the fracture parameter W_c was allocated to each integration point in order to obtain a normal distribution.

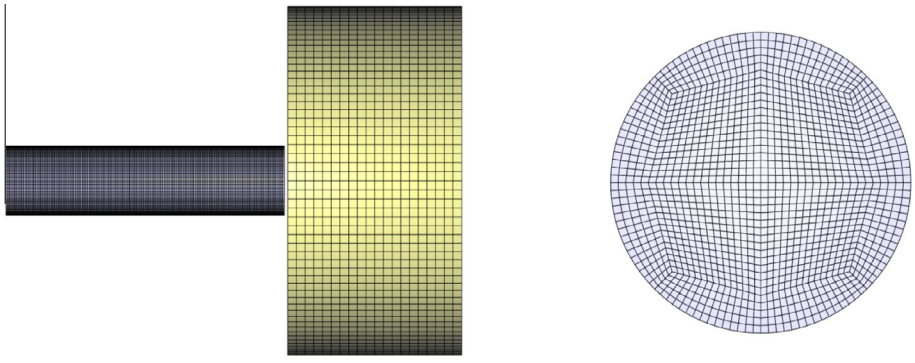

Fig. 8. The mesh used in numerical simulations of Taylor bar impact tests: (a) shows the projectile and anvil from the side, (b) shows a cross-section of the longitudinal mesh through the projectile.

Table 6
Deformed mushroom diameter, maximum damage, maximum plastic strain and maximum temperature shown as results of varying anvil and friction parameters.

	No friction	Friction law	Friction	No friction	Friction law	Friction law
	Mushroom diameter [mm]			Maximum damage [–]		
Rigid	36.9	34.8	34.1	1.64	1.40	1.30
Elastic	36.4	34.1	33.7	1.16	0.97	0.91
Plastic	35.4	33.2	32.8	1.12	0.88	0.82
	Maximum plastic strain [–]			Maximum temperature [K]		
1.98	1.60	1.55	833	743	730	
1.89	1.41	1.38	809	690	681	
1.64	1.24	1.22	749	645	639	

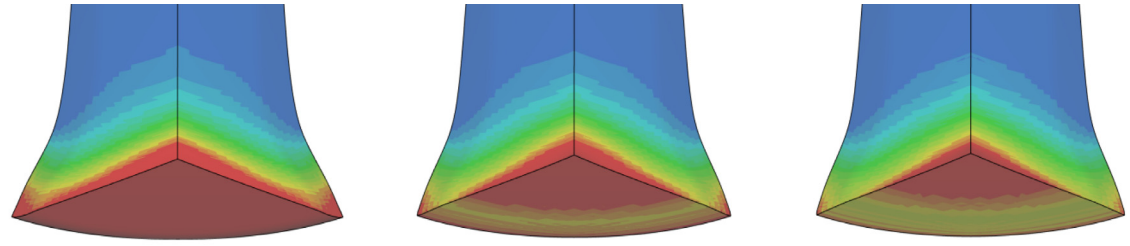

(a) Rigid anvil – no friction (b) Rigid anvil – friction law (c) Rigid anvil – constant friction

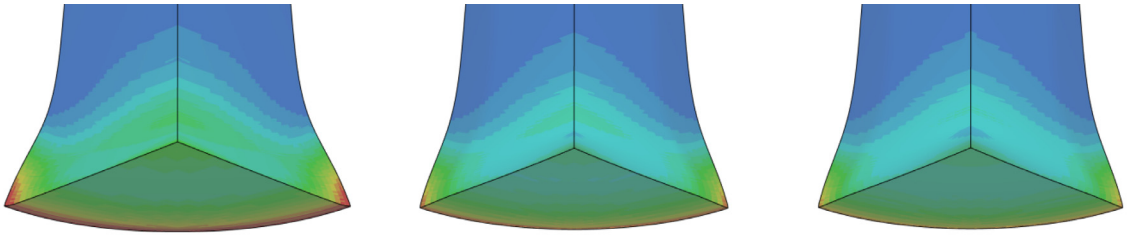

(d) Elastic anvil – no friction (e) Elastic anvil – friction law (f) Elastic anvil – constant friction

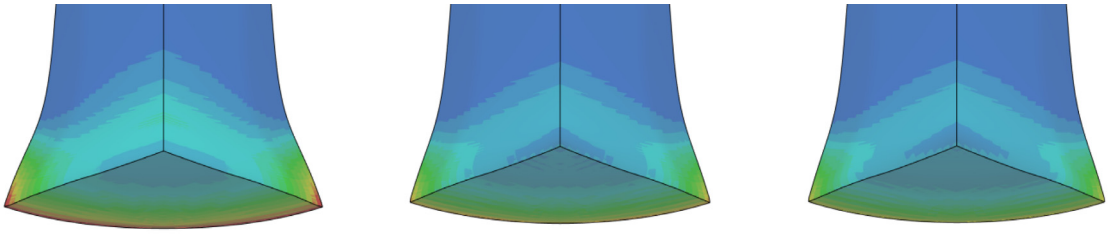

(g) Plastic anvil – no friction (h) Plastic anvil – friction law (i) Plastic anvil – constant friction

Fig. 9. Longitudinal quarter section cuts of the projectiles with three different anvil properties and three different friction properties. Contours of the damage variable are plotted from 0 to 1.

5.1. Influence of friction and anvil deformation

As discussed in the Introduction, there are two assumptions in Taylor's analysis that are not always justified, namely a rigid anvil and a frictionless contact surface. These assumptions are reasonable for doing simplified, analytical calculations, but are unfortunately often also employed in numerical simulations. If friction is respected, a constant friction value of 0.1 is often used, see e.g. Teng et al. (2005).

The unhardened projectile with the highest impact velocity that did not fracture (297.2 m/s – see Table 1) is used in the following to study how the assumptions regarding friction and anvil properties affect the numerical results. Regarding the anvil properties, the anvils used in the experiments (Rakvåg et al., 2013) had a hardness

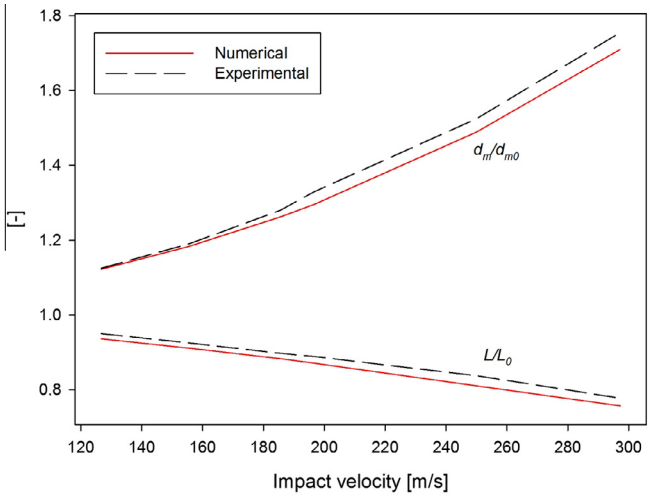

Fig. 10. Comparison between experimental and predicted plastic deformations of the unhardened projectiles vs. impact velocity.

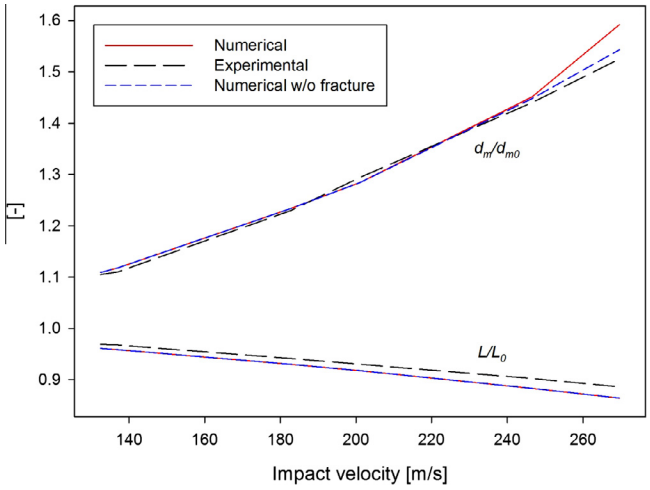

Fig. 12. Comparison of the experimental and predicted plastic deformations of the HRC 40 projectiles at impact velocities where severe fracture did not occur in the experiments.

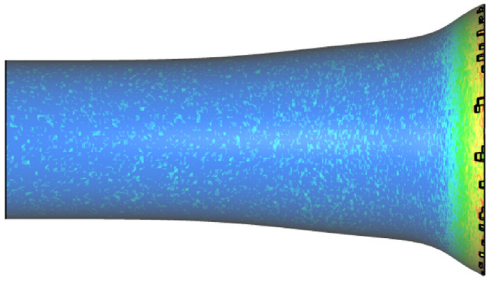

(a) Heterogeneous model, impact velocity 297.2 m/s

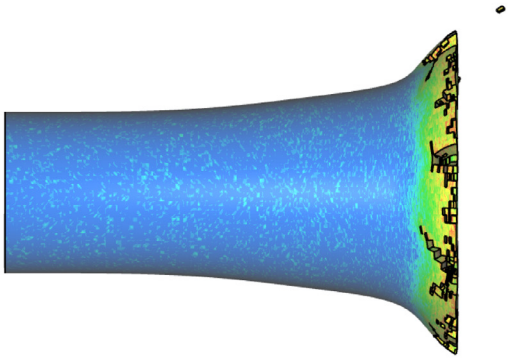

(b) Heterogeneous model, impact velocity 341.4 m/s

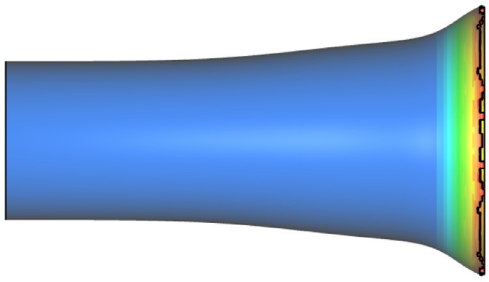

(c) Homogeneous model, impact velocity 297.2 m/s

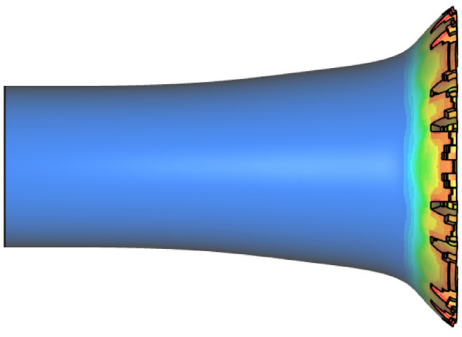

(d) Homogeneous model, impact velocity 341.4 m/s

Fig. 11. Fracture modes of the unhardened projectiles as predicted by heterogeneous and homogeneous fracture criteria. Simulations with an impact velocity 297.2 m/s are shown to the left, while simulations with an impact velocity of 341.4 m/s are shown to the right. Contours of the damage variable are plotted from 0 to 1.

value of HRC 60, corresponding to a compressive yield strength of approximately 2150 MPa according to the producer (Uddeholm, 2012). The material behaviour of the anvil was not determined experimentally, so details of work hardening and other characteristics are not known. Therefore, three different variations of the anvil material behaviour were simulated with increased complexity: rigid, elastic and elastic–plastic with yield strength of 2150 MPa and some minor hardening for numerical stability.

In addition, three different friction properties were investigated: no friction, a constant friction coefficient of 0.1 and a yield-limited friction law. The yield-limited law for the friction coefficient υ is written as

$$\upsilon = \min\left(\upsilon_0, \frac{\tau_{max}}{P_{contact}}\right) \tag{12}$$

where υ_0 is the initial friction coefficient, τ_{max} is the maximum allowed interfacial shear stress and $P_{contact}$ is the contact pressure. This approach is inspired from metal forming (Hosford and Caddell, 1993) where the interfacial shear stress can be assumed to be limited by the yield strength in shear. Here this approach is used with conservative yield strength in shear of 100 MPa and an initial friction coefficient of 0.1.

The unhardened projectile with an impact velocity of 297.2 m/s was chosen for this investigation, because it had no visible exterior

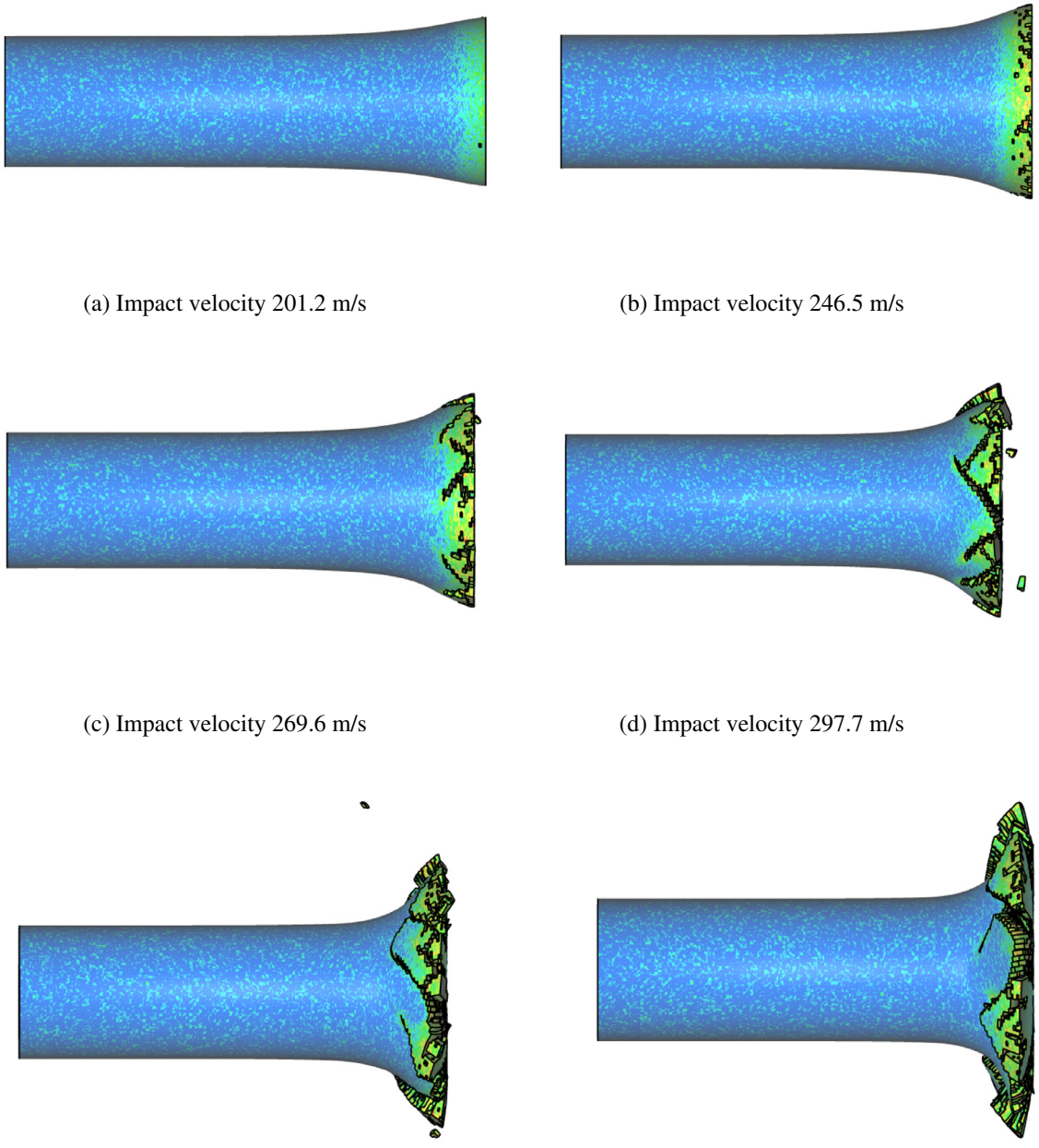

(a) Impact velocity 201.2 m/s

(b) Impact velocity 246.5 m/s

(c) Impact velocity 269.6 m/s

(d) Impact velocity 297.7 m/s

(e) Impact velocity 325.6 m/s

(f) Impact velocity 356.5 m/s

Fig. 13. Fractures modes of the HRC 40 projectiles as predicted by the numerical simulations for impact velocities of 201.2 up to 356.5 m/s. Contours of the damage variable are plotted from 0 to 1.

cracks and it was also checked for interior excessive void growth (Rakvåg et al., 2013). It is then known that the damage should be less than, but probably close to, unity in the numerical simulations. From Table 1 we also know the experimental mushroom diameter to be 35.1 mm. In these particular simulations, homogeneous fracture properties are assumed in order to have directly comparable results. Accordingly, the fracture parameter W_c is uniform and equal to 535 MPa. The damage D is allowed to grow beyond unity without element erosion in these simulations.

The results are shown in Table 6, where the mushroom diameter and maximum damage are shown for all nine combinations of anvil and friction properties. Maximum plastic strain and maximum temperature are also included even though no experimental results are available as for deformed mushroom diameter and damage. Note that nothing else than the anvil and friction properties are changed, and still the variation in mushroom diameter is more than 10%. The maximum damage for the case with rigid anvil and no friction is found to be double the damage in the case with plastic anvil and constant friction. The results are even more interesting when fringes of the damage D are plotted on the deformed configuration as shown in Fig. 9. All plots have the same fringe scale from zero to unity, meaning that red equals a damage level above unity. Considerable variation in the maximum value, extent and distribution of damage is observed.

All the simulations with a rigid anvil have a large extent of damage above unity, and the damage is most excessive at the centre of the impact end. This seems unphysical with respect to the experimental observation that cracks start at the rim of the projectile. The sets of simulations with elastic and elasto-plastic anvil have a different damage distribution, which is more coherent with the experimental results. Regarding the deformed mushroom diameter, the results with an elastic anvil is closer to the results with a rigid anvil than the results with an elasto-plastic anvil. The maximum plastic strain and the maximum temperature show the same trend as the maximum damage, namely that uncertain boundary conditions can change the results with almost 100%.

For this particular case, it is also seen that some friction is required to reduce the damage below unity for all three anvil configurations. Of the simulations with damage less than unity, the simulation with an elastic anvil and a yield-limited friction law has the mushroom diameter which is closest to the experimental value of 35.1 mm. Thus, these conditions are chosen for the remainder of the simulations throughout this work. Based on these results there seems to be no justification for assuming a rigid anvil in numerical simulations of Taylor bar impact tests when the elastic constants are known. It should be noted that very small dents were also observed in the anvil after impact in some of the experimental tests (Rakvåg et al., 2013), indicating that the anvil behaviour was plastic, but since the hardening parameters are not known elastic behaviour is used.

5.2. Simulations of the unhardened projectiles

Results from the simulations of the unhardened projectiles up to the highest impact velocity without visible fracture are shown in Fig. 10, together with the experimental results from Table 1. The results are shown as normalised mushroom diameter d_m/d_{m0} and normalised length L/L_0, where d_m and L are the deformed mushroom diameter and length while d_{m0} and L_0 are the initial diameter and length of the projectile. All simulations are run with an elastic anvil and a yield-limited friction law as described in the previous section, and matched with the heterogeneous damage model presented in Section 4.2. As seen from Fig. 10, the plastic deformations of the projectile are predicted with good accuracy and are well within the uncertainty of the boundary conditions discussed in the previous section. An interesting observation is

Fig. 14. HRC 40 projectiles after impact at velocities of 297.7, 325.6, and 356.6 m/s, respectively.

that the simulations consistently overestimate the shortening of the cylinder and underestimates the mushrooming at the impact end of the projectiles. Due to the plastic incompressibility, this indicates that the profile of the projectile is not predicted correctly. A possible reason for this could be the strain rate sensitivity, which is calibrated for strain rates up to 10^3 s^{-1} and extrapolated to strain rates at the order of 10^5 s^{-1}, which occur in simulations of the projectile with impact velocity of 297.2 m/s.

The critical impact velocity from the experiments is somewhere between 297.2 and 341.4 m/s. The experiment at 297.2 m/s had no visible signs of fracture or voids, while the experiment at 341.4 m/s resulted in tensile splitting and spiral shear. From the numerical simulations, the lowest impact velocity simulated where elements are eroded is 297.2 m/s. At this velocity a few elements are eroded at the rim of the projectile, but without coalescing into distinct cracks. As for the simulations of projectiles impacting at 341.4 m/s, both spiral shear and tensile splitting are present in the projectile, in close agreement with the experimental result.

The main advantage of using a heterogeneous fracture criterion comes into light when the aforementioned results are compared with simulations using a deterministic and homogeneous fracture criterion. Fig. 11 shows projectiles after impact from both simulations with heterogeneous and homogenous fracture characteristics. It is evident that the heterogeneous fracture criterion predicts the fracture modes more accurately, especially the spiral shear at impact velocity of 341.4 m/s. It should also be noted that the heterogeneous model distributes the damage in a much better

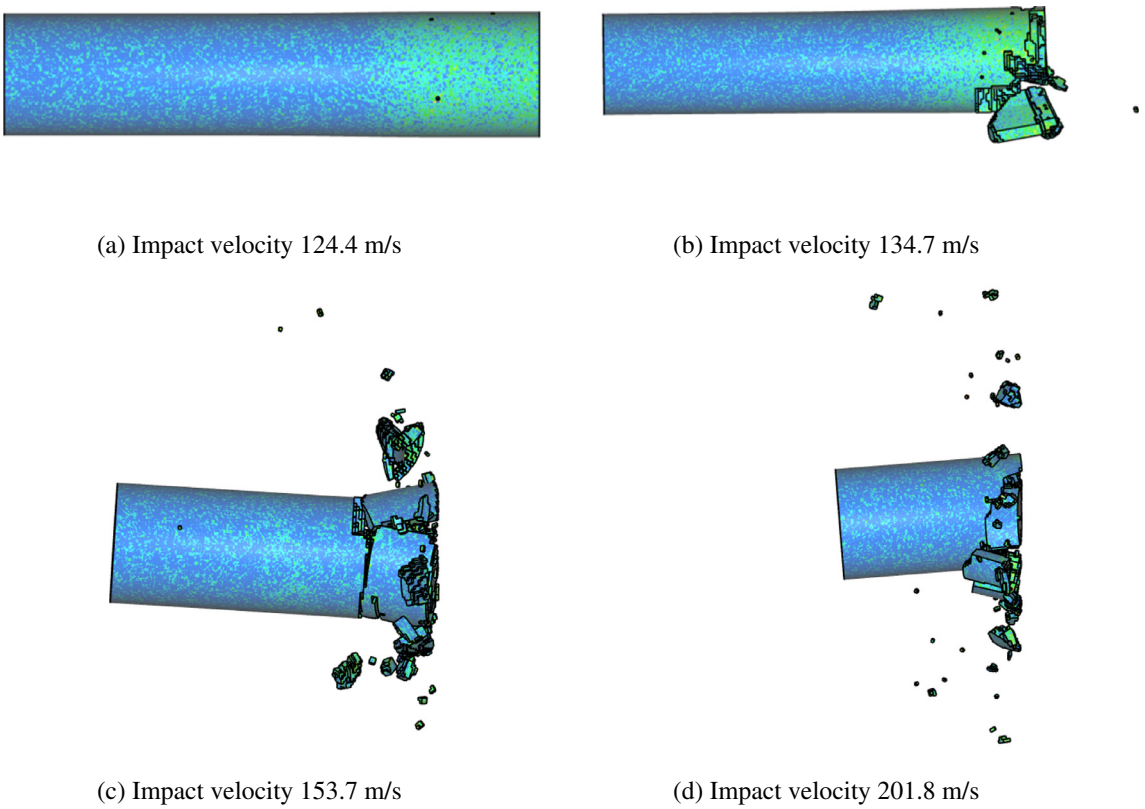

(a) Impact velocity 124.4 m/s

(b) Impact velocity 134.7 m/s

(c) Impact velocity 153.7 m/s

(d) Impact velocity 201.8 m/s

Fig. 15. Numerical simulations of HRC 52 projectile at impact velocities 124.4, 134.7, 153.7, and 201.8 m/s. Contours of the damage variable are plotted from 0 to 1.

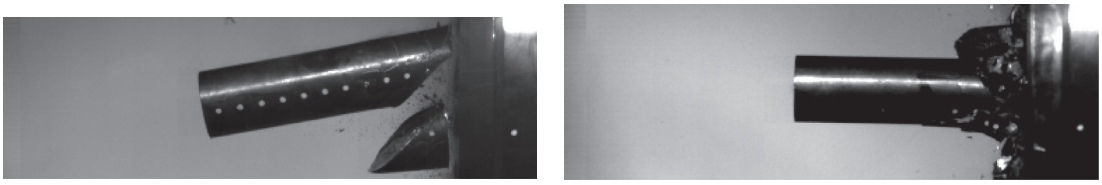

(a) Impact velocity 134.7 m/s

(b) Impact velocity 153.7 m/s

Fig. 16. HRC 52 projectile captured by the high-speed video camera: (a) impact at 132.9 m/s where the fracture mode is principal shear fracture, and (b) impact at 153.7 m/s where the projectile fragments.

way than the homogeneous model, where broad bands of damage near unity is present in the vicinity of the already eroded elements.

5.3. Simulations of the HRC 40 projectiles

Plots of the normalised length and normalised mushroom diameter, as defined previously, for the HRC 40 projectiles are shown in Fig. 12. Impact velocities up to 269.9 m/s are included, which is the velocity of tensile splitting from the experimental results. It is seen that the mushroom diameter diverges from the experimental results at high impact velocity. This is due to element erosion appearing already at an impact velocity of 201.2 m/s. Because of this, a second set of simulations was run without a fracture criterion to check if the hardening parameters are still valid. The results from these simulations are also shown in Fig. 12, and it is seen that the predicted mushroom diameter follows the trend from the experimental values and that the deformed length of the projectile is not influenced by fracture confined to the rim of the projectile. Again, the shortening of the projectile is consistently overestimated by the numerical simulations, while the mushrooming is satisfactorily reproduced, especially considering that the strain rate sensitivity parameter is just assumed based on the unhardened material.

Regarding the fracture modes from the simulations, it is already mentioned that element erosion starts to appear at impact velocities as low as 201.2 m/s, while the lowest impact velocity giving visible fracture from the experiments is 269.9 m/s where tensile splitting appeared (see Table 1). The computed fracture modes from the numerical simulations are shown in Fig. 13. Even though a couple of elements erode in the simulations at an impact velocity of 201.2 m/s, it could not be considered as a definitive fracture. At 246.5 m/s enough elements are eroded at the rim of the projectile that it should be considered as tensile splitting. Simulations of the projectile that impacted at 269.6 m/s, i.e. the velocity of tensile splitting from the experiments, result in a combination of spiral shear and tensile splitting. Simulations at impact velocities of 297.7 m/s and above are in close agreement with the experimental results shown in Fig. 14. At an impact velocity of 297.7 m/s, the spiral shear cracks start to coalesce, resulting in fragments being ejected from the projectile. In both the experiments and the simulations excessive distortion of the mushroom periphery occurs at an impact velocity of 356.5 m/s.

Table 7
Typical percentage eroded mass in HRC 52 simulations at different impact velocities.

Impact velocity	124.4 m/s	132.9 m/s	153.7 m/s	201.8 m/s
Eroded mass	0.01%	3%	30%	55%

Thus, the established numerical model is capable of representing the plastic deformation of the projectile in good agreement with the experimental results, and is also capable of recreating the relevant fracture modes – even though the critical impact velocity for projectile failure is found to be slightly lower in the simulations than in the experiments. However, this is coherent with the simulations of the unhardened projectiles, which also exhibited a slightly lower critical velocity than the experiments.

5.4. Simulations of the HRC 52 projectiles

The results from the Taylor bar impact test simulations of the HRC 52 projectiles are shown in Fig. 15. In the experiment with impact velocity 124.4 m/s no visible cracks or fractures were observed. The same result is predicted by the numerical simulations, except for a few deleted elements away from the impact end. This is probably due to the standard deviation of 20% of the mean value for the HRC 52 projectiles (see Table 4), giving the possibility that an element is close to failure already at the start of the analysis.

The critical velocity is predicted in the same range as found in the experiments, since the simulations of impact at 132.9 m/s predict fracture. An asymmetrical principal shear crack akin to the experimental observation is reproduced in some of the simulations at this velocity. The experimentally observed principal shear crack is shown in Fig. 16.

At velocities of 153.7 m/s and above, fragmentation is predicted in the simulations. This is also in accordance with the experimental results, where fragmentation started at an impact velocity of 153.7 m/s and gets more excessive with increased impact velocity. However, the numerical simulations do not capture well the fragmentation process, because substantial erosion of the projectile takes place. In the simulations at an impact velocity of 201.8 m/s, more than half the mass is eroded, rendering the simulations of less value for design applications.

In Table 7 typical percentages of the projectile mass that is eroded in the numerical simulations are shown for the different impact velocities. At impact velocities that result in fragmentation of the projectile, an unacceptable percentage of the mass is eroded. So even though the model is capable of predicting crushing, it is likely to underestimate the momentum transferred to a protective structure because of the massive erosion of the mass of the projectile.

6. Discussion and conclusions

The aim of this work has been to show that incorporation of observed heterogeneous material properties into numerical analysis gives a better description of the various failure processes in the Taylor bar impact test than using a homogeneous material description. The approach is based on the observed macro-mechanical variation of the failure strain in tensile tests. To represent this behaviour in the simulations, the fracture parameter was defined as a random variable with a normal distribution.

With respect to the distribution, this approach differs from most others where the failure properties are distributed adopting a Weibull distribution. The use of a Weibull distribution is based on the statistics of microcracks (Ruggieri and Dodds, 1996), and allows for the volume effect, namely that there is a greater probability of finding a large defect in a large volume than in a small one. In the current study, the volume effect is not included, and finite elements of the same characteristic size are used in the calibration of the material properties and in the subsequent simulations of the Taylor bar impact tests.

The proposed approach is capable of reproducing all the experimentally observed fracture modes, except for massive fragmentation which is not reproduced satisfactorily because of excessive element erosion. However, the fragment distribution is less important in the design of protective structures because the penetration capability of the projectile diminishes when fragmentation occurs (Dey et al., 2011). Element erosion is the *de facto* standard for introducing cracks in commercial finite element codes, but the method introduces some non-physical effects.

The erosion algorithm used herein is rather simple, where the entire element is removed when the failure criterion is first reached in one of the eight integration points of the solid element. This has the unphysical consequence of reducing the mass and introducing a zero pressure void, with the possible effect of allowing pressure redistribution from the surrounding material (Johnson et al., 2002). A possible remedy for this is to let the element sustain compressive hydrostatic stresses while the deviatoric stresses are set to zero (Børvik et al., 2011). This will, however, result in excessively distorted elements with concomitant small time-steps. Another approach is to convert distorted elements to meshless particles as in Johnson et al. (2002), at the cost of added complexity in the simulations.

A returning problem with element erosion is its intrinsic mesh-dependency. Recently, an eigenerosion approach for brittle fracture was proposed to enhance the convergence properties of element erosion techniques (Pandolfi and Ortiz, 2012). In the present work, the problem is minimized by using the same element size and formulation in the simulations used to determine the material properties and in the subsequent simulations of the Taylor bar impact tests. This implies that the element size is a parameter in the modelling of fracture. Similar approaches have been employed in various applications to model ductile fracture, e.g. Ruggieri et al. (1996) and Xue et al. (2010). Alternatives to element erosion for simulation of fracture and fragmentation exist, such as node splitting (Komori, 2001), but they are still not verified for general applications in 3D numerical simulations.

In this study element erosion was employed, as it is available in most commercial explicit finite element codes, unlike node splitting or particle conversion. Other approaches, like keeping the compressive hydrostatic stresses, introduce for practical reasons purely numerical parameters, such as a criterion for eroding elements when they cause intolerably small time-steps. The time-dependency of fracture, as discussed in the Introduction, was not investigated here. The reason for this is the lack of experimental data to support the simulations. Solid elements with selective-reduced integration were used in this study, which implies that each element has eight integration points. It was here chosen to erode the element as the first integration point reached the failure criterion. An advantage with this choice is that overly distorted elements, due to reduced load-carrying capacity by damage, are avoided, thus keeping a reasonable time step throughout the simulations. However, also the number of integration points that reaches the critical damage value before the finite element is eroded should be considered as a numerical parameter.

The fracture parameter was assumed as a random variable governed by a normal distribution in the simulations. The available experimental data are not sufficient to support this choice, and the normal distribution was adopted mainly due to its simplicity. We believe that the distribution itself is essential, not the particular form of it. This was supported by an earlier work where a three-part discrete distribution was successfully employed (Rakvåg et al., 2012).

Except from the discussed problems with element erosion, the proposed model with a normal distribution of the fracture parameter based on macro-mechanical observations is shown to reproduce experimentally observed fracture modes and critical velocities with good accuracy. Also, common assumptions regarding anvil behaviour and friction properties are shown to be possible sources of error in numerical simulations of Taylor bar impact tests.

Acknowledgments

The financial support of this work from the Structural Impact Laboratory (SIMLab), Centre for Research-based Innovation (CRI) at the Norwegian University of Science and Technology (NTNU), is gratefully acknowledged. The authors would also like to thank Dr. Torodd Berstad for his contribution with the numerical implementation of the constitutive relation and failure criterion.

References

Anderson, C.E., 1987. An overview of the theory of hydrocodes. Int. J. Impact Eng. 5, 33–59.
Anderson, C.E., Chocron, I.S., Nicholls, A.E., 2006. Damage modeling for Taylor impact simulations. J. De Phys. IV 134, 331–337.
Antoun, T., Seaman, L., Curran, D.R., Kanel, G.I., Razorenov, S.V., Utkin, A.V., 2003. Spall Fracture. Springer, New York.
Bao, Y., Wierzbicki, T., 2004. On fracture locus in the equivalent strain and stress triaxiality space. Int. J. Mech. Sci. 46, 81–98.
Beremin, F.M., 1983. A local criterion for cleavage fracture of a nuclear pressure vessel steel. Metall. Trans. A 14, 2277–2287.
Bertholf, L.D., Buxton, L.D., Thorne, B.J., Byers, R.K., Stevens, A.L., Thompson, S.L., 1975. Damage in steel plates from hypervelocity impact. II. Numerical results and spall measurements. J. Appl. Phys. 46, 3776–3783.
Børvik, T., Hopperstad, O.S., Berstad, T., Langseth, M., 2001. A computational model of viscoplasticity and ductile damage for impact and penetration. Eur. J. Mech. A. Solid 5, 685–712.
Børvik, T., Hopperstad, O.S., Langseth, M., Malo, K.A., 2003. Effect of target thickness in blunt projectile penetration of Weldox 460 E steel plates. Int. J. Impact Eng. 28, 413–464.
Børvik, T., Hopperstad, O.S., Dey, S., Pizzinato, E.V., Langseth, M., Albertini, C., 2005. Strength and ductility of Weldox 460 E steel at high strain rates, elevated temperatures and various stress triaxialities. Eng. Fract. Mech. 72, 1071–1087.
Børvik, T., Dey, S., Clausen, A.H., 2009. Perforation resistance of five different high-strength steel plates subjected to small-arms projectiles. Int. J. Impact Eng. 36, 948–964.
Børvik, T., Olovsson, L., Dey, S., Langseth, M., 2011. Normal and oblique impact of small arms bullets on AA6082-T4 aluminium protective plates. Int. J. Impact Eng. 38, 577–589.
Carrington, W.E., Gayler, M.L.V., 1948. The use of flat-ended projectiles for determining dynamic yield stress. III. Changes in microstructure caused by deformation under impact at high-striking velocities. Proc. R. Soc. London, Ser. A 194, 323–331.
Cockcroft, M.G., Latham, D.J., 1968. Ductility and workability of metals. J. Inst. Metals 96, 33–39.
Dey, S., Børvik, T., Hopperstad, O.S., Leinum, J.R., Langseth, M., 2004. The effect of target strength on the perforation of steel plates using three different projectile nose shapes. Int. J. Impact Eng. 30, 1005–1038.
Dey, S., Børvik, T., Teng, X., Wierzbicki, T., Hopperstad, O.S., 2007. On the ballistic resistance of double-layered steel plates: an experimental and numerical investigation. Int. J. Solids Struct. 44, 6701–6723.
Dey, S., Børvik, T., Hopperstad, O.S., 2011. Computer-aided design of protective structures: numerical simulations and experimental validation. Appl. Mech. Mater. 82, 686–691.
Dieter, G.E., 1988. Mechanical Metallurgy. McGraw-Hill, London.
Gruben, G., Hopperstad, O.S., Børvik, T., 2012. Evaluation of uncoupled ductile fracture criteria for the dual-phase steel Docol 600DL. Int. J. Mech. Sci. 62, 133–146.
Gurson, A.L., 1975. Plastic flow and fracture behaviour of ductile materials incorporating void nucleation, growth, and interaction, Ph.D. thesis, Brown University.
Hosford, W.F., Caddell, R.M., 1993. Metal Forming: Mechanics and Metallurgy. New Jersey Prentice-Hall.
IMPETUS-AFEA, 2013. [Internet]. Flekkefjord, Norway: IMPETUS Afea AS; c2013 [cited 2013 July 10]. IMPETUS Afea Solver, <http://www.impetus-afea.com/solver>.
Johnson, W.E., 1972. Impact Strength of Materials. Edward Arnold Ltd, London.
Johnson, W.E., Anderson, C.E., 1987. History and application of hydrocodes in hypervelocity impact. Int. J. Impact Eng. 5, 423–439.
Johnson, G.R., Cook, W.H., 1983. A constitutive model and data for metals subjected to large strains, high strain rates and high temperatures. In: Proc. 7th Int. Symp. on Ballistics, The Hague, The Netherlands, April 1983, pp. 541–547.
Johnson, G.R., Cook, W.H., 1985. Fracture characteristics of three metals subjected to various strains, strain rates, temperatures and pressures. Eng. Fract. Mech. 21, 31–48.
Johnson, G.R., Stryk, R.A., Beissel, S.R., Holmquist, T.J., 2002. An algorithm to automatically convert distorted finite elements into meshless particles during dynamic deformation. Int. J. Impact Eng. 27, 997–1013.
Johnson, G.R., Holmquist, T.J., Anderson, C.E., Nicholls, A.E., 2006. Strain-rate effects for high-strain computations. J. Phys. IV 134, 391–396.
Kane, A., Børvik, T., Berstad, T., Hopperstad, O.S., 2011. Failure criteria with unilateral conditions for simulation of plate perforation. Eur. J. Mech. A. Solid 30, 468–476.
Komori, K., 2001. Simulation of shearing by node separation method. Comput. Struct. 79, 197–207.
Le Roy, G., Embury, D., Edwards, G., Ashby, M.F., 1981. A model of ductile fracture based on the nucleation and growth of voids. Acta Metall. Mater. 29, 1509–1522.
LS-DYNA, 2006. LS-DYNA theory manual, vol. 971. Livermore Software Technology Corporation.
Lund, J.R., Byrne, J.P., 2001. Leonardo Da Vinci's tensile strength tests: implications for the discovery of engineering mechanics. Civ. Eng. Environ. Syst. 18, 243–250.
Meyer, H.W., Brannon, R.M., 2012. A model for statistical variation of fracture properties in a continuum mechanics code. Int. J. Impact Eng. 42, 48–58.
Mirone, G., 2004. A new model for the elastoplastic characterization and the stress–strain determination on the necking section of a tensile specimen. Int. J. Solids Struct. 41, 3545–3564.
Mott, N.F., 1947. Fragmentation of shell cases. Proc. R. Soc. A. Math. Phys. 189, 300–308.
Pandolfi, A., Ortiz, M., 2012. An eigenerosion approach to brittle fracture. Int. J. Numer. Methods Eng. 92, 694–714.
Rakvåg, K.G., Børvik, T., Hopperstad, O.S., Westermann, I., 2012. Experimental and numerical study on fragmentation of steel projectiles. In: Proceedings DYMAT 10, Freiburg.
Rakvåg, K.G., Børvik, T., Westermann, I., Hopperstad, O.S., 2013. An experimental study on the deformation and fracture modes of steel projectiles during impact. Mater. Des. 51, 242–256.
Ruggieri, C., Dodds, R.H., 1996. A transferability model for brittle fracture including constraint and ductile tearing effects: a probabilistic approach. Int. J. Fract. 79, 309–340.
Ruggieri, C., Panotin, T.L., Dodds, R.H., 1996. Numerical modeling of ductile crack growth in 3-D using computational cell elements. Int. J. Fract. 82, 67–95.
Taylor, G., 1948. The use of flat-ended projectiles for determining dynamic yield stress. I. Theoretical considerations. Proc. R. Soc. London Ser. A 194, 289–299.
Teng, X., Wierzbicki, T., Hiermaier, S., Rohr, I., 2005. Numerical prediction of fracture in the Taylor bar impact test. Int. J. Solids Struct. 42, 2929–2948.
Timoshenko, S.P., 1953. History of Strength of Materials: With a Brief Account of the History of Theory of Elasticity and Theory of Structure. McGraw-Hill, New York.
Tuler, F.R., Butcher, B.M., 1968. A criterion for the time dependence of dynamic fracture. Int. J. Fract. Mech. 4, 431–437.
Uddeholm, 2012. [Internet]. Hagfors, Sweden: Uddeholms AB; [updated 2012 September; cited 2013 June 18]. Uddeholm Arne; [pdf, 12 pages], <http://www.uddeholm.com/files/PB_Uddeholm_arne_english.pdf>.
Whiffin, A.C., 1948. The use of flat-ended projectiles for determining dynamic yield stress. II. Tests on various metallic materials. Proc. R. Soc. London, Ser. A 194, 300–322.
Wilkins, M.L., Guinan, M.W., 1973. Impact of cylinders on a rigid boundary. J. Appl. Phys. 44, 1200–1206.
Xiao, X., Zhang, W., Wei, G., Mu, Z., Guo, Z., 2011. Experimental and numerical investigation on the deformation and failure behavior in the Taylor bar impact test. Mater. Des. 32, 2663–2674.
Xue, Z., Pontin, M.G., Zok, F.W., Hutchinson, J.W., 2010. Calibration procedures for a computational model of ductile fracture. Eng. Fract. Mech. 77, 492–509.
Zerilli, F.J., Armstrong, R.W., 1987. Dislocation-mechanics-based constitutive relations for material dynamics calculations. J. Appl. Phys. 61, 1816–1825.
Zhang, W., Xiao, X., Wei, G., Guo, Z., 2011. Evaluation of five fracture models in Taylor impact fracture. AIP Conf. Proc. 1426, 1125–1128.